



The nanostructure preservation of 3D porous graphene: New insights into the graphitization and surface chemistry of non-stacked double-layer templated graphene after high-temperature treatment



Jia-Le Shi ^a, Hao-Fan Wang ^a, Xiaolin Zhu ^a, Cheng-Meng Chen ^b, Xing Huang ^c,
Xiao-Dong Zhang ^d, Bo-Quan Li ^a, Cheng Tang ^a, Qiang Zhang ^{a,*}

^a Beijing Key Laboratory of Green Chemical Reaction Engineering and Technology, Department of Chemical Engineering, Tsinghua University, Beijing 100084, China

^b Key Laboratory of Carbon Materials, Institute of Coal Chemistry, Chinese Academy of Sciences, 27 Taoyuan South Road, Taiyuan 030001, China

^c Key Laboratory of Photochemical Conversion and Optoelectronic Materials, Technical Institute of Physics and Chemistry, Chinese Academy of Sciences, 29 Zhongguancun East Road, 100190 Beijing, China

^d Environment and Low-Carbon Research Center, School of Environment and Architecture, University of Shanghai for Science and Technology, Shanghai 200093, China

article info

Article history:

Received 21 November 2015

Received in revised form

16 February 2016

Accepted 1 March 2016

Available online 4 March 2016

abstract

Three-dimensional (3D) porous graphene materials with few layer nature and non-stacked structural feature afford significant advantages in high electrical conductivity, large surface area, and interconnected porous nanostructures. However, the structure evolution of porous graphene under high temperature is poorly understood. In this contribution, 3D double-layer templated graphene (DTG) composed of two non-stacked graphene layers with interlayer spacing around 15 nm and separated by a large quantity of protuberances, was employed as a special case to track the structure evolution of 3D porous graphene at high temperature. Compared with thermally reduced graphene oxide with easy graphitized nature, the unique non-stacked DTG structure was well preserved after a high-temperature annealing at 1600 °C. With limited self-healing of defects for graphene layers, and with preservation of mesosized protuberances that prevent graphene layers stacking during annealing, DTG is regarded as 'hard carbon' ('non-graphitizable carbon'). The electron microscopy, Raman spectroscopy, X-ray diffraction spectroscopy, X-ray photoelectron spectroscopy, thermogravimetric analysis, gravimetric elemental analysis, nitrogen/water physisorption, and probe reactions of electrochemical oxygen reduction reaction were employed to reveal the graphitization degree and surface chemistry of non-stacked DTG after high-temperature treatment.

© 2016 Elsevier Ltd. All rights reserved.

1. Introduction

Graphene is an important material platform for vast applications in energy storage, electrocatalysis, environmental protection, chemical conversion, as well as nanoelectronics. However, the facile stacking nature induced by the strong π - π interaction and van der Waals forces between graphene layers hinders the full demonstration of intrinsic properties of graphene. Recent efforts to build three-dimensional (3D) porous graphene have demonstrated significantly enhanced performance due to increased surface area

and much more effective pores to transport and/or store electrons/ions/reactants/active phases for its bulk use in many devices [1e5].

Liquid phase exfoliation, thermal reduction of graphite oxide (GO), and chemical vapor deposition (CVD) are the dominate methods for bulk production of 3D porous graphene [6]. For instance, the thermally reduced graphene oxide (rGO) that was exfoliated from GO via facile thermal treatment inherited few layer stacking character from the GO precursor as well as afforded the tunable surface area and electronic conductivity at the same time [7,8]. The 3D porous graphene aerogels can be achieved through hydrothermal reduction with cross-linker molecules [9,10]. The 3D porous graphene fabricated through high-temperature CVD growth has controllable architectures and large graphene domains [11,12].

* Corresponding author.

E-mail address: zhang-qiang@mails.tsinghua.edu.cn (Q. Zhang).

For instance, 3D macroscopic graphene foams were easily fabricated on Ni foam substrate through CVD growth [12]. The use of metal/oxide template and gas/solid carbon sources is an efficient route to achieve 3D porous graphene for supercapacitors [3,13,14], biosensors [15], Li ion batteries [16], and LiES batteries [17,18]. Recently, we reported double-layer templated graphene (DTG) with two non-stacked graphene layers separated by numerous meso-sized protuberances extending from the graphene layers (Fig. 1a) [19]. Such DTG affords impressive properties in the field of supercapacitors, batteries, and electrocatalysis [19e21].

As the high-temperature process is commonly applied in commercial graphite production, two different types of carbon materials are distinguished by their graphitization behaviors. They are hard carbon (non-graphitizable carbon, such as glassy carbon, Ketjen black, etc) [22,23] and soft carbon (graphitizable carbon, such as petroleum pitch, mesophase carbon micro beads, etc) [24e26]. Recently, the rGO-based graphene macro-assembly results from Worsley et al. manifested the graphitizable characteristic [8], indicating such rGO can be easily graphitized at high-temperature. 3D porous graphene fabricated through CVD is mostly fabricated at 850e1200 °C. The high-temperature (>1200 °C) annealing of CVD grown porous graphene has not been extensively studied yet. Consequently, whether CVD grown 3D porous graphene materials is classified as soft carbon or hard carbon is still an open question.

In this contribution, the structure evolution of 3D porous DTG grown by CVD has been investigated after high-temperature (1600 °C) treatment. The rGO fabricated through thermal reduction of GO was applied as control sample. The evolution of both graphitization degree and surface chemistry is probed through atomic force microscopy (AFM), Raman spectroscopy, X-ray diffraction spectroscopy (XRD), X-ray photoelectron spectroscopy (XPS), thermogravimetric analysis (TGA), gravimetric elemental analysis, and nitrogen/water physisorption. We find CVD grown DTG is inclined to hard carbon, while rGO is classified as soft carbon. Electrocatalytic oxygen reduction reaction (ORR) is selected as a probe reaction to monitor the surface chemistry of graphene nanostructures before and after 1600 °C annealing. The oxygen-containing functional groups have been almost removed and their electrochemical reactivity is significantly modulated by the high-temperature treatment.

2. Experimental

2.1. Material synthesis

The synthesis of DTG was carried out by a high-temperature (950 °C) catalytic CVD with MgAl-layered double oxides (LDOs) as

templates. The LDOs were obtained by the calcination of MgAl-layered double hydroxides (LDHs), which has been described in our previous publication (Fig. 1a) [19]. The yield of DTG on LDO template was ca. 0.12 g_{DTG}/g_{LDO}. After graphene deposition, the raw products were purified by hydrothermal reactions with 15.0 M NaOH aqueous solution at 180 °C for 12.0 h and subsequent treatment with HCl (5.0 M) aqueous solution at 80 °C for 12.0 h. The MgAl-LDOs were fully removed, and DTG with two non-stacked graphene sheets were achieved. After filtering, washing, and freeze-drying, the 3D porous DTG flakes were finally obtained.

The rGO was obtained by rapid heating up of GO under vacuum atmosphere (Fig. 1b) [7]. The GO powder was placed into the center of a tube furnace. The quartz tube with GO was pre-evacuated to pressure less than 5.0 Pa, and then heated up to 1000 °C with a heating rate of 30 °C min⁻¹. The high-temperature thermal reduction was maintained for 20 min before the furnace was cooled to room temperature. The as-obtained rGO sample possessing honeycomb-like porous graphene structure with randomly enlarged interlayer spacing was named G1000 [7].

To investigate the high-temperature annealing behavior of 3D porous graphene materials, both DTG and G1000 were subjected to a vacuum annealing at 1600 °C, 10⁻¹ Pa for 2.0 h. The as-obtained samples were named DTG-1600C and G1000-1600C, respectively.

2.2. Structure characterizations

The morphology of samples were characterized by a JSM 7401F field-emission scanning electron microscope (SEM, JEOL, Japan) at 3.0 kV and a JEM 2010 high solution transmission electron microscope (TEM, JEOL, Japan) at 120.0 kV. The high resolution TEM observation at atomic level was performed on an aberration-corrected JEM-ARM200F TEM (JEOL, Japan) with a cold field emitter. The AFM images were obtained using NanoMan VS scanning probe microscope system with NanoScope V controller (Veeco, USA). X-ray diffraction (XRD) patterns were recorded on a D8 Advance diffractometer equipped with a Cu-K_α radiation source (Bruker, USA). Raman spectra of the graphene samples was collected with a HeeNe laser excitation at 633 nm using LabRAM HR800 Raman spectrophotometer (Horiba Jobin Yvon, France). Thermogravimetric analysis (TGA) was performed by the TGA/DSC1 STAR[®] system (Mettler Toledo, Switzerland) with a temperature ramp rate of 20 °C min⁻¹ and O₂ flow rate of 50 mL min⁻¹. Both N₂ and water isotherms were collected at -196 °C (77 K) and 20 °C (293 K) respectively with a volumetric Autosorb-IQ₂-MP-C system (Quantachrome, USA). The specific surface area (SSA) was determined by the BrunauerEmmetteTeller (BET) method. The pore size distributions were calculated using the quenched solid density functional theory method from the adsorption branches of the N₂

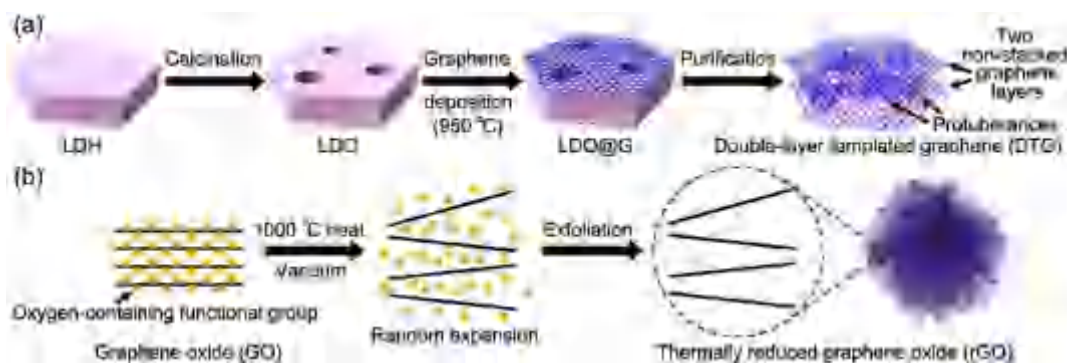


Fig. 1. Scheme for the synthesis of (a) DTG and (b) rGO. (A color version of this figure can be viewed online.)

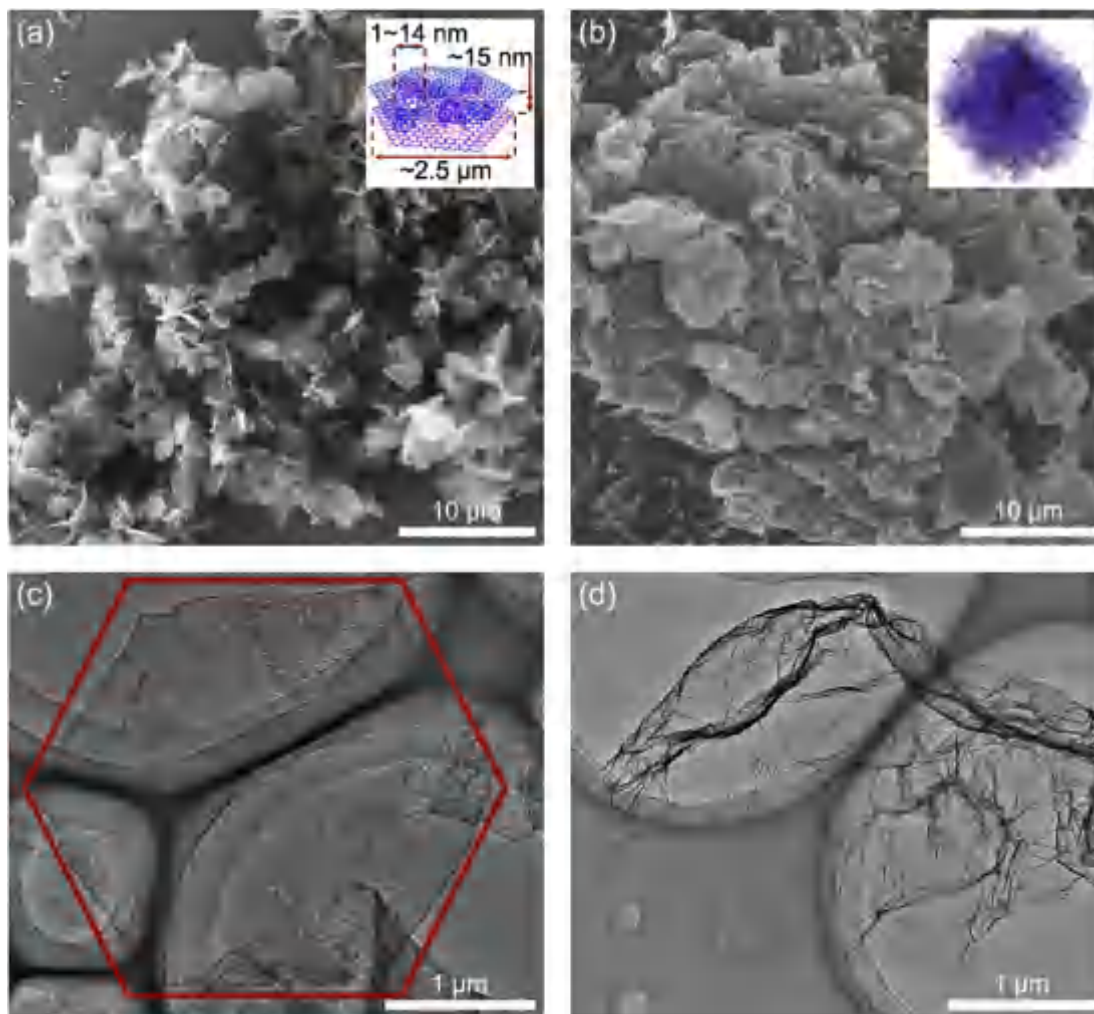


Fig. 2. Morphological characterization of the DTG and G1000. SEM images of (a) the DTG and (b) G1000 (structural model inset); TEM images of (c) the DTG and (d) G1000. The structural model of DTG and G1000 were insets of Fig. 2a and b, respectively. In order to facilitate the identification, the size ratio of up/down graphene layers to protuberances was distorted in the DTG model. However, the actual size is labeled in the inset of Fig. 2a. (A color version of this figure can be viewed online.)

isotherms. Before the physisorption measurements, the sample was degassed at 300 °C for 10.0 h. The XPS operated by EscaLab 250Xi (Thermo Fisher Scientific Inc., USA) was employed to determine the amount of oxygen-containing functional groups in the samples. The gravimetric elemental analysis was performed on a Vario EL III Elemental Analyzer (Elementar Analysensysteme GmbH, Germany).

2.3. Electrocatalytic performance evaluation

The evaluation of the electrocatalytic performance of all the samples was carried out in a three-electrode electrochemical cell with a saturated calomel electrode (SCE) and a platinum foil as the reference and the counter electrode, respectively. The graphene samples were loaded onto a rotating ring-disk electrode (RRDE) to serve as the working electrode with a mass loading of 255 mg cm⁻². Typically, 5.0 mg catalyst was dispersed in a mixture solution of 0.95 mL ethanol and 50.0 mL Nafion solution (5.0 wt%) under ultrasonication. 10.0 mL catalyst solution was pipetted onto the 5.0 mm diameter glassy carbon disk electrode. The working electrode was fabricated after the evaporation of solvent.

The evaluation tests were performed at room temperature using 0.10 mol L⁻¹ O₂-saturated KOH as electrolyte. A CHI 760D

electrochemical workstation was employed to record the experimental data (Shanghai Chenhua, China). RRDE voltammogram measurements were conducted on a RRDE configuration (Pine Research Instrument, USA). The disk electrode was scanned cathodically at 10 mV s⁻¹ and the potential of the Pt ring electrode was set at +0.5 V constantly. The electron transfer number *n* were determined as followed:

$$n = \frac{4I_d}{I_d + I_r} = N \quad (1)$$

where *I_d* is disk current, *I_r* is ring current and *N* is current collection efficiency of the Pt ring which was determined to be 0.26.

3. Results and discussion

3.1. Nanostructures of DTG

Both DTG and rGO (G1000) were annealed at 1600 °C for 2.0 h. There are a large amount of mesosized carbon protuberances to prevent stacking of two graphene layers in DTG that cast conformally from oxide template of calcined LDH with abundant of Kirkendall voids (Figs. 1a and 2a) [19,20]. Compared with rGO

prepared by vacuum promoted thermal exfoliation of GO with spitball-like bulk morphology (Figs. 1b and 2b) [7], the DTG flakes clearly segregate from each other (Fig. 2a). DTG flakes with a lateral size of ca. 2.5 μm (Fig. 2c) are well replicated from the hexagon morphology of their LDH precursors. In contrast, rGO sample (G1000) possesses honeycomb-like porous graphene structure with randomly enlarged interlayer spacing (Fig. 2d) [7].

The SEM and AFM images shown in Fig. S1a-b reveals that the DTG exhibits a thickness of ca. 15 nm, indicating the distance of the two graphene layers in DTG are enlarged to ca. 14.3 nm by short carbon protuberances (Fig. S1c). The introduction of protuberances as pillars in DTG is a very effective strategy to prevent the stacking of up/down graphene layers. After 2.0 h high-temperature annealing, the hexagon flake morphology is well preserved (Fig. 3a and Fig. S2) and the thickness of DTG-1600C is still around 15 nm (Fig. 3b), which confirms the thermal stability of carbon protuberances serving as the pillars inside the 3D porous graphene.

The TEM image of the DTG-1600C exhibits a large number of protuberances on surface of the graphene (Fig. 3c) that prevents the stack of the two graphene layers deposited on both sides of the oxide templates. The cap of protuberance is closed like carbon

nanotube, the root of protuberance is covalently bonded with the flat graphene layer (inset of Fig. 3c), in these two parts pentagonal and heptagonal carbon rings formed and preserved indicates remaining high-density defects on DTG after 1600 $^{\circ}\text{C}$ annealing. The high-resolution TEM image displays the large-size graphene domains in one piece of DTG-1600C (Fig. 3d). Because of the high-temperature self-healing, there is no outstanding pore on the graphene layer, which guarantees the high electrical conductivity of the as-obtained DTG-1600C.

Because of the presence of protuberances on the surface of graphene, the π - π interactions between graphene layers are significantly weakened, which prevents the up/down neighboring layers of DTG stacking to a certain extent. The microscopical analysis of DTG and DTG-1600C provides direct evidence to support the good preservation of non-stacked 3D porous graphene structure after high-temperature treatment. This indicates the good structural stability of DTG, which is similar to the routine hard carbon materials.

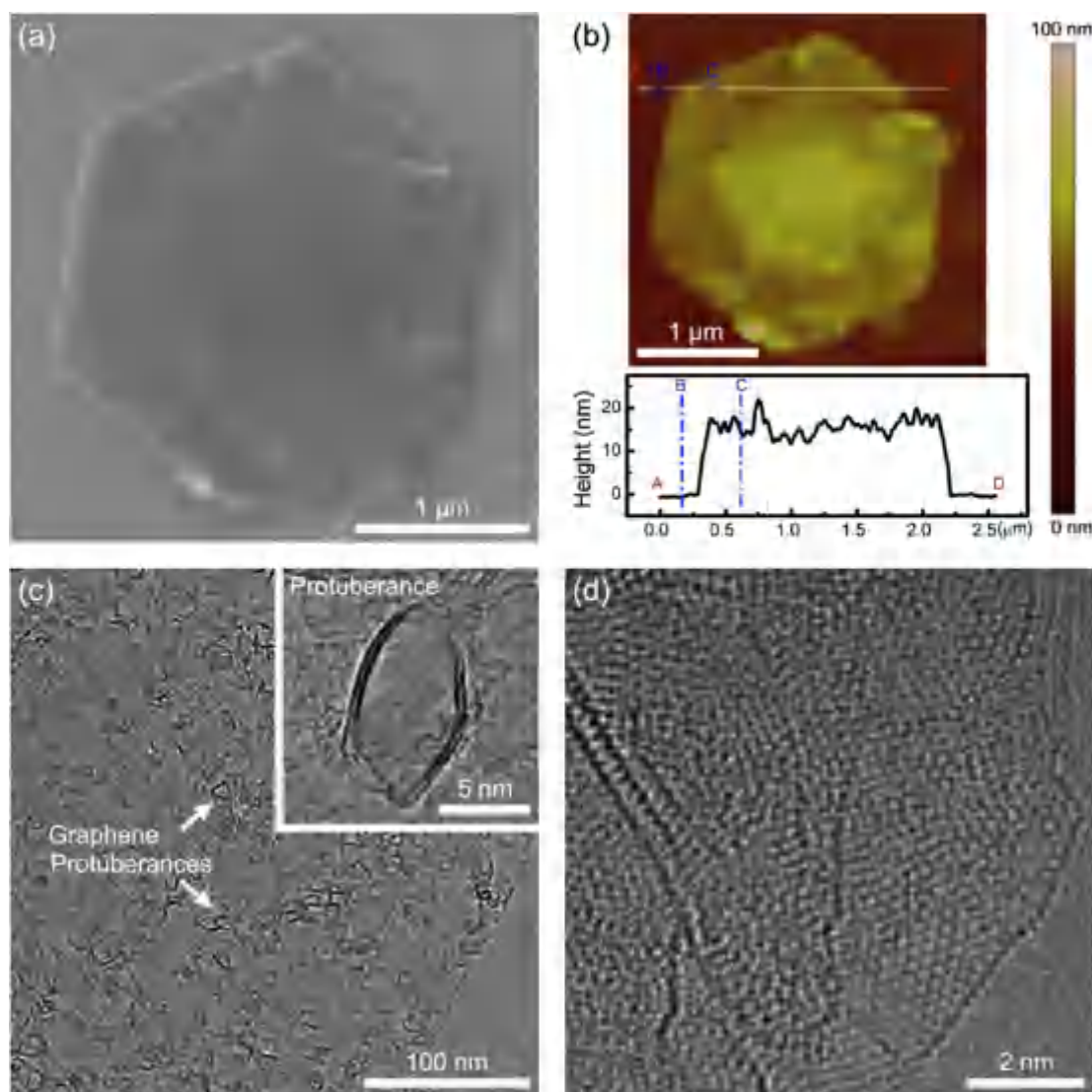


Fig. 3. Morphological characterization of the DTG-1600C. (a) SEM image and (b) AFM image of the DTG-1600C; (c) TEM image of the DTG-1600C with carbon protuberances extending from the graphene layer; (d) high-resolution TEM image of graphene layer in the DTG-1600C. (A color version of this figure can be viewed online.)

3.2. Comparison of graphitization degree in annealed DTG and rGO

To investigate the orderly stacking degree of graphene layers and defect density in bulk samples, N_2 physisorption, XRD, and Raman spectra were employed in this contribution. The rGO (G1000) sample was also employed as a control sample to indicate the importance of intrinsic non-stacked 3D porous graphene nanostructures for their superb stability at high temperature.

The stable nanostructure of 3D porous graphene is firstly investigated by N_2 physisorption test. The N_2 isotherms of both DTG and DTG-1600C exhibit a sharp increase at $P/P_0 < 0.05$ and a dominant hysteresis loop at $P/P_0 > 0.35$, indicating a hierarchically micro- and mesoporous structure (Fig. 4a). As N_2 prefers to adsorb on defects, wrinkles, and functional groups of graphene at low relative pressure ($P/P_0 < 0.05$) [27], the decrease of adsorbing volume ($P/P_0 < 0.05$) after annealing is attribute to the loss of microporous adsorption sites (defects, wrinkles, and functional groups of graphene) through 'self-healing' of graphitic lattice. The calculated pore size distribution of the DTG(-1600C) indicates abundant mesopores with size ranging from 3 to 15 nm (Fig. 4b), which is mainly contributed from the mesoporous space between up and down graphene layers of the as-prepared DTG(-1600C). The 0.6e1.0 nm micropores of DTG almost disappear, while most mesopores are well preserved after 1600 °C treatment.

The N_2 isotherm of G1000 was also collected (Fig. S3a). Both the isotherm shape and pore size distribution of G1000/G1000-1600C are quite different from those of DTG/DTG-1600C (Fig. S3a-b). The

G1000/G1000-1600C exhibit a small microporous adsorbing volume at $P/P_0 < 0.05$ because of the lower defect density from exfoliation of graphite. The graphene sheets with randomly enlarged interlayer spacing reestablish ordered stacking again after 1600 °C annealing. This reduces the proportion of 4e11 nm pores decrease and the pore volume to drop from 2.93 (G1000) to 2.54 $cm^3 g^{-1}$ (G1000-1600C) after annealing (Fig. S3b). The SSA of DTG (1600 $m^2 g^{-1}$) and DTG-1600C (1071 $m^2 g^{-1}$) reported herein is larger than G1000 (723 $m^2 g^{-1}$) and G1000-1600C (435 $m^2 g^{-1}$). Both the TEM image (Fig. 3c) and the N_2 physisorption confirm the good preservation of protuberances in DTG. These results directly support the superb stability of the 3D nanostructure in DTG at very high temperature.

XRD is a facile characterization tool to characterize crystalline orientation and defects, as well as interlayer spacing disorder of graphene layers [28]. Similar XRD patterns of DTG and DTG-1600C have been illustrated by Fig. 4c. The graphite, bilayer or multilayer graphene with long-range ordered stacking (interlayer spacing around 0.334 nm, called (002) crystal face) of graphene layers afford strong X-ray reflection around $q = 26.5$. The tiny, weak, and broad (002) peak of DTG demonstrates the fact that the distance between up and down neighboring DTG graphene layers didn't orderly stack into ca. 0.334 nm. On the contrary, relatively obvious (002), (100), and (101) peaks of G1000 become much sharper after 1600 °C graphitization. Restacking of randomly distributed graphene sheets in G1000 is unambiguously confirmed well, while the non-stacked nature of DTG has been validated again based on bulk

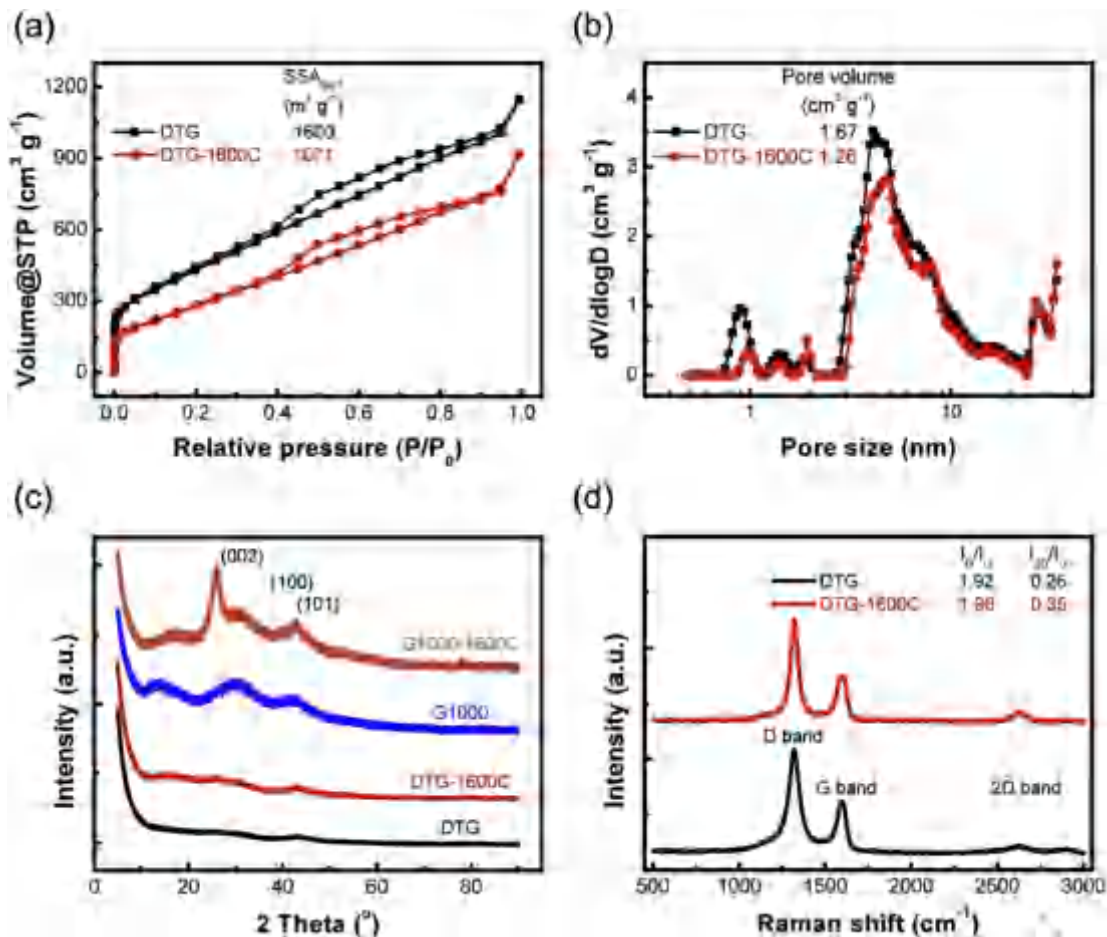


Fig. 4. Structural characterization of the DTG and DTG-1600C. (a) N_2 isotherms of the DTG and DTG-1600C; (b) Pore size distributions derived from isothermal adsorption plots; (c) XRD patterns of the DTG, DTG-1600C, G1000, and G1000-1600C; (d) Raman spectra of the DTG and DTG-1600C. (A color version of this figure can be viewed online.)

samples. The nanostructure of DTG has been well preserved, which is inclined to be hard carbon. In contrast, the rGO can be classified as soft carbon.

To gain more detailed information on the defect evolution during high-temperature annealing, Raman spectra of both DTG and G1000 were collected. DTG exhibits high intensity ratio of D band to G band (I_D/I_G) of 1.92, which is associated with the presence of a large quantity of five- and six-membered carbon rings for the tops of short protuberances and covalent connections between the protuberances and the graphene layer (Fig. 4d). Combined with a simultaneous 'self-healing' of graphitic lattice and the continuous deoxygenation for topological defects generation, DTG-1600C has a similar I_D/I_G value of 1.96. Meanwhile, both DTG and DTG-1600C exhibit low ratios of 2D band to G band (I_{2D}/I_G) with 0.26 and 0.35, respectively. The broad 2D band reveals up/down graphene layers of DTG(-1600C) is not AB-Bernal stacking [29], while the weak intensity of 2D band reflects its single-layer nature. As for G1000, however, the I_D/I_G ratio decreases, the I_{2D}/I_G ratio increases, and three peaks sharpen remarkably after 1600 °C treatment. The re-graphitization of G1000 occurs not only in the graphene layers with defunctionalization and defect healing, but also among adjacent graphene layers with restacking and more rotational order (Fig. S3c).

3.3. The surface chemistry of DTG and rGO after high-temperature treatment

The properties of graphene-based materials are not only inherent from their nanostructures, but also linked to their surface chemistry. In most cases, the edges of the graphene nanosheets are always saturated with an abundance of oxygen-containing functional groups. The reactivity of graphene edges with oxygen under gas or liquid atmosphere is also strongly determined by their nanostructures. To gain a full scenario of 3D porous graphene during high-temperature annealing, the surface chemistry was firstly probed by XPS, then oxidation behavior and water physisorption of samples were carried out to identify the role of defects and oxygen-containing functional groups in these graphene materials.

The relative abundance of oxygen and/or hydrogen on the surface of graphene samples was listed as Fig. 5a and Table 1. After annealing of DTG and G1000 in high vacuum at 1600 °C, the oxygen content on graphene surface significantly decreases from 5.22 at.% of DTG and 1.45 at.% of G1000 to 2.23 at.% of DTG-1600C and 0.90 at.% of G1000-1600C, respectively. The inset of Fig. 5a exhibited the C1s fine scan spectra of graphene samples. The C1s peak of G1000-1600C became sharper and more symmetric than that of G1000, indicating high degree of graphitization. While compared with DTG, the C1s peak of DTG-1600C just sharpened a little bit for reduced content of heteroatom. As for the O1s fine scan spectra, the following bonds were assigned as C=O (531.65–531.94 eV) and CeO (533.30–533.80 eV) [30]. There are significant changes in composition of oxygen-containing functional groups on surface of DTG and G1000 after high-temperature treatment (Fig. 5b and Fig. S4). The composition of the graphene sample was also validated through the gravimetric elemental analysis. The amounts of carbon, hydrogen, and oxygen were calculated through thermal conductivity detector (TCD) of the oxidation products CO₂ and H₂O. The results listed in Table 1 reveal the consistent decrease tendency of oxygen content from 5.51 to 0.97 wt.% for DTG and 2.22 to 0.47 wt.% for G1000, respectively.

TGA measurements in O₂ atmosphere were performed on these graphene materials. The DTG and G1000 became more resistant to the O₂ combustion reaction after high-temperature annealing (Fig. 5c). The differential plot of thermogravimetric curves reflected

weight loss rate during the test (inset Fig. 5c). The improvement of 120 °C from 559 to 679 °C in thermal stability of G1000 is due to the decreased defect density of the highly crystalline few-layer graphene, which is larger than the improvement of 51 °C from 592 to 643 °C for non-stacked DTG with more exposed surface area and less graphitization underwent.

The water physisorption behavior at 293 K was depended on both 3D texture and surface chemistry, which is a sensitive reflection of the hydrophilic or hydrophobic property of graphene interfaces [31]. The water isotherms of graphene materials are shown in Fig. 5d. The decreased water vapor adsorption volume of DTG and G1000 after annealing is ascribed to the more hydrophobic surface and loss of surface area after deoxygenation and defect healing. It should be noticed that the DTG-1600C exhibits more water physisorption capacity than G1000-1600, which is related with the surface properties of the 3D porous graphene samples.

Gathering the results through XPS, TGA, and water physisorption tests, we found the loss of oxygen-containing functional groups during the high-temperature annealing. Due to many intrinsic graphene defects in the 3D porous graphene and good preservation of the architectures, the amount of residual oxygen heteroatoms in DTG-1600C is two times larger than those in G1000-1600C. The hard carbon like DTG has more anchoring sites for C=O and CeO, consequently, the DTG-1600C with more oxygen functional groups affords more adsorption sites for water physisorption shown in Fig. 5d.

3.4. The electrocatalytic performance of DTG after high-temperature treatment

Rational design of oxygen electrode catalysts for ORR is the key to a wide range of renewable energy technologies such as fuel cells, metal-air batteries, etc [32]. However, ORR is kinetically sluggish due to the complicated multi-electron transfer process, which induces severe energy efficiency loss. Nanocarbon materials as noble-metal-free electrocatalysts for ORR have attracted great attentions [33,34]. The ORR activity of carbon materials is generally ascribed to (1) the charge localization or spin-polarization of the carbon atoms covalently bonded with the dopants [35]; (2) edge-site carbon atoms, dangling bonds, and topological defects as high-energy sites for charge redistribution [36]. In this contribution, ORR was selected as the probe reaction for non-stacked DTG and G1000 to explore the structure–function relationship before and after annealing.

With the structural information, we are able to establish association between the oxygen-containing functional groups, structural defects of graphene materials and the ORR electrocatalysis. Fig. 6a reveals the linear sweep voltammetry profiles on a RRDE. All the catalysts afford ORR current while with different onset potentials and current densities. The onset potentials of DTG, G1000, DTG-1600C, and G1000-1600C catalysts are –0.135, –0.135, –0.170, and –0.220 V, respectively. The onset potential of graphene electrode is positively shifted compared to that of annealed graphene with +35 mV for DTG and +85 mV for G1000, which is mainly ascribed to the loss of active sites as well as the contact surface area.

Higher oxygen content, more structure defects as active sites, more hydrophilic surface area, and effective conductive networks render DTG electrode possessing higher reaction current than that of G1000. Similarly, DTG-1600C exhibits much improved ORR reactivity than G1000-1600. This indicates the loss of the active centers for ORR on both DTG and G1000 induced by the loss of oxygen-containing functional groups. However, the defect-rich DTG samples with more oxygen-containing functional groups always render higher ORR current before/after heat treatment. This

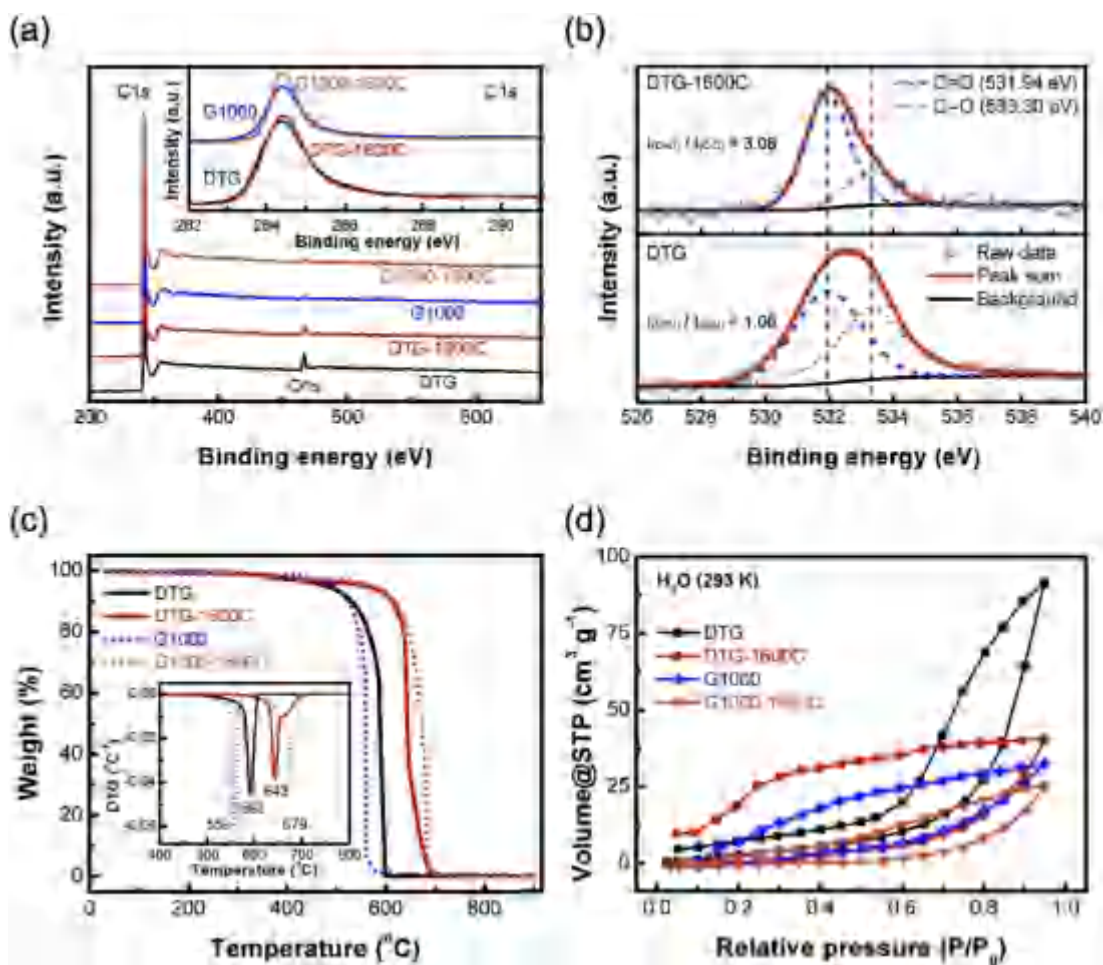


Fig. 5. Surface chemistry of the DTG and DTG-1600C. (a) XPS spectra of DTG, G1000, DTG-1600C, and G1000-1600C; inset of (a) the C1s fine scan spectra; (b) The O1s fine scan spectra of DTG (bottom) and DTG-1600C (top). (c) The TGA curves, differential plots (inset) and (d) the water isotherms of 3D porous graphene samples. (A color version of this figure can be viewed online.)

Table 1
A summary of the elemental composition of 3D porous graphene samples.

Method	XPS (surface)			Elemental analysis (bulk)				
	C (at.%)	O (at.%)	C/O atom ratio	C (wt.%)	H (wt.%)	O (wt.%)	C/O atom ratio	C/H atom ratio
DTG	94.78	5.22	18.16	93.81	0.68	5.51	22.72	11.49
DTG-1600C	97.77	2.23	43.84	98.66	0.37	0.97	135.41	22.31
G1000	98.55	1.45	67.97	96.63	1.15	2.22	58.04	7.00
G1000-1600C	99.10	0.90	110.11	99.07	0.46	0.47	279.25	17.87

provides an indirect evidence to support the non-stacked nature of DTG which affords more active centers for ORR.

The ring currents collected at +0.5 V shown in Fig. 6a are induced by the oxidation of HO_2^- produced on the working electrode. This revealed the contrary relationship upon disk currents, which suggested more 2-electron pathway occupied in ORR on DTG and DTG-1600C electrode. The calculated electron transfer number of ORR on graphene electrodes (Fig. 6b) reveals such relationship attributed to different kinds of oxygen-containing functional groups [37,38] and localized charge separation at the interface [39]. After high-temperature annealing, the loss of functional groups and self-annealing of defects lead to decrease of active centers. Even the DTG-1600C sample have more pillars between two neighboring graphene layers, a 2-electron dominant ORR behavior is recorded, which was the result of the two competition reaction pathways: the

oxygen-containing functional groups play a dominate role towards 4-electron ORR, while the preserved defects after high-temperature annealing contributes to 2-electron electrocatalysis process for ORR [40].

The ORR results reported herein further confirmed the loss of oxygen-containing functional groups during the high-temperature annealing, which is consisted with XPS and element analysis results. Compare with ORR current on G1000-1600C, the higher activity of DTG-1600C is attributed from more intrinsic defects as well as strong water absorbance confirmed by vapor sorption experiments. Confirmed with AFM images and various characterization methods, the non-stacked DTG is stable at a temperature of 1600 °C, whose behavior is inclined to be 'hard carbon'. In contrast, G1000 prefers to be soft carbon, which is easy to be graphitized and lose their surface area. The DTG exhibits a much improved

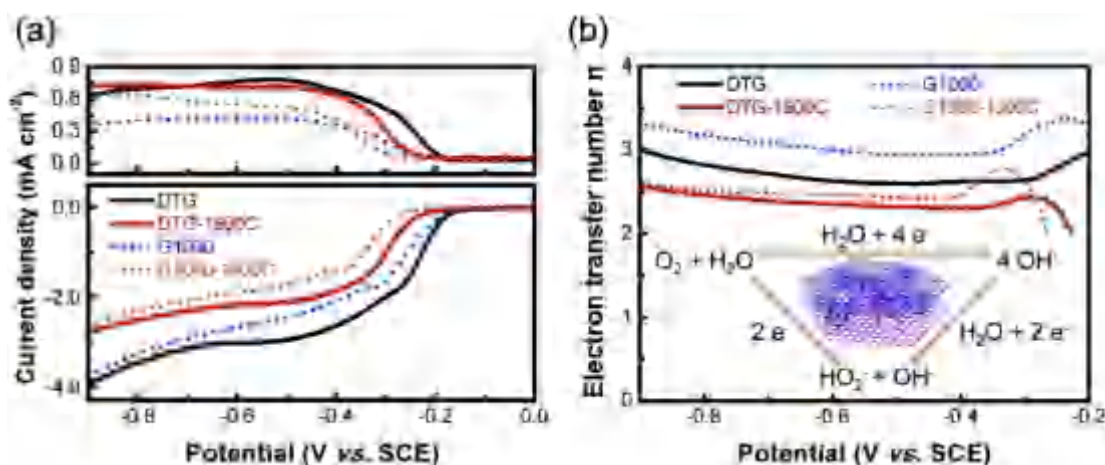


Fig. 6. The ORR performance of graphene catalysts. (a) Linear sweep voltammetry plots of disk current densities (bottom) and the corresponding ring current densities (top) of DTG, G1000, DTG-1600C, and G1000-1600C catalysts on RRDE in O_2 -saturated 0.1 mol L^{-1} KOH solution; (b) the electron transfer number of the DTG, G1000, DTG-1600C, and G1000-1600C catalysts based on the corresponding RRDE data in (a), the inset exhibited the possible reaction pathways of ORR in aqueous alkaline electrolyte. (A color version of this figure can be viewed online.)

structural stability, although its oxygen-containing functional groups were significantly lost at a high annealing temperature.

4. Conclusions

A comparative investigation of high-temperature ($1600 \text{ }^\circ\text{C}$) evolution of CVD grown graphene (DTG) and reduced graphene oxide (G1000) has been carried out. The AFM, TEM images verified the robust non-stacked DTG structure with ca. 14.3 nm interlayer spacing are well preserved at the high-temperature $1600 \text{ }^\circ\text{C}$. A dominant $3 \times 15 \text{ nm}$ mesopores is detected, which is corresponding to the DTG structure feature of carbon pillars between up and down graphene layers. The SSA of DTG-1600C ($1071 \text{ m}^2 \text{ g}^{-1}$) maintains from that of DTG ($1600 \text{ m}^2 \text{ g}^{-1}$) on account of the non-stacked porous structure, while the SSA of thermally reduced GO is significantly decreased from 723 to $425 \text{ m}^2 \text{ g}^{-1}$ after high temperature annealing. The nearly invariable XRD patterns and Raman spectra of DTG(-1600C) indicates the limited defects self-healing and non-graphitizable nature for the two non-stacked graphene layers in DTG. The nanostructures have been well preserved in DTG, which is preferred to be a 'hard carbon'. In contrast, the rGO can be classified as 'soft carbon'. There were significantly changes on the surface chemistry of both DTG and rGO. As verified by the TGA, XPS, bulk elemental analysis, and water physisorption behavior, most of oxygen-containing functional groups (with $<1 \text{ wt}\%$ O left) have been removed during high-temperature treatment. Compared with thermally reduced graphene oxide of G1000 with easy graphitized nature, non-stacked DTG with more hydrophilic surface area and defects induced high-energy sites exhibited better ORR activity before and after annealing. We should notice that whether CVD graphene is a hard carbon may have different answers since the graphitization behavior of CVD graphene is depended on CVD grown methods (e.g. multilayered graphene nanosheets with long-range order can be easily grown on Ni substrate while non-stacked graphene nanosheets are achieved in DTG grown on mesoporous LDO template). With the already extensive and broad usage of 3D porous graphene materials in applications area of composites and energy conversion, the availability of 3D porous graphene facilitates significant performance enhancements and bulk applications of novel 'hard carbon' for Na-ion batteries, supercapacitors, electrocatalysis, environmental protection, and so on.

Acknowledgments

This work was supported by the Natural Scientific Foundation of China (No. 21306102 and 21422604) and Tsinghua University Initiative Scientific Research Program (2014z22076). The authors thank Mr. Xin-Feng Wu for his service on high temperature furnace.

Appendix A. Supplementary data

Supplementary data related to this article can be found at <http://dx.doi.org/10.1016/j.carbon.2016.03.002>.

References

- [1] L.L. Jiang, Z.J. Fan, Design of advanced porous graphene materials: from graphene nanomesh to 3D architectures, *Nanoscale* 6 (2014) 1922e1945.
- [2] S. Han, D. Wu, S. Li, F. Zhang, X. Feng, Porous graphene materials for advanced electrochemical energy storage and conversion devices, *Adv. Mater* 26 (2014) 849e864.
- [3] X.H. Cao, Z.Y. Yin, H. Zhang, Three-dimensional graphene materials: preparation, structures and application in supercapacitors, *Energy Environ. Sci.* 7 (2014) 1850e1865.
- [4] S. Mao, G.H. Lu, J.H. Chen, Three-dimensional graphene-based composites for energy applications, *Nanoscale* 7 (2015) 6924e6943.
- [5] Y.X. Xu, G.Q. Shi, X.F. Duan, Self-assembled three-dimensional graphene macrostructures: synthesis and applications in supercapacitors, *Accounts Chem. Res.* 48 (2015) 1666e1675.
- [6] K.S. Novoselov, V.I. Falko, L. Colombo, P.R. Gellert, M.G. Schwab, K. Kim, A roadmap for graphene, *Nature* 490 (2012) 192e200.
- [7] C.M. Chen, Q. Zhang, M.G. Yang, C.H. Huang, Y.G. Yang, M.Z. Wang, Structural evolution during annealing of thermally reduced graphene nanosheets for application in supercapacitors, *Carbon* 50 (2012) 3572e3584.
- [8] M.A. Worsley, T.T. Pham, A. Yan, S.J. Shin, J.R.I. Lee, M. Bagge-Hansen, et al., Synthesis and characterization of highly crystalline graphene aerogels, *ACS Nano* 8 (2014) 11013e11022.
- [9] H.Y. Sun, Z. Xu, C. Gao, Multifunctional, ultra-flyweight, synergistically assembled carbon aerogels, *Adv. Mater* 25 (2013) 2554e2560.
- [10] H. Hu, Z.B. Zhao, W.B. Wan, Y. Gogotsi, J.S. Qiu, Ultralight and highly compressible graphene aerogels, *Adv. Mater* 25 (2013) 2219e2223.
- [11] H.J. Peng, J.Y. Liang, L. Zhu, J.Q. Huang, X.B. Cheng, X.F. Guo, et al., Catalytic self-limited assembly at hard templates: a mesoscale approach to graphene nanoshells for lithium-sulfur batteries, *ACS Nano* 8 (2014) 11280e11289.
- [12] Z.P. Chen, W.C. Ren, L.B. Gao, B.L. Liu, S.F. Pei, H.M. Cheng, Three-dimensional flexible and conductive interconnected graphene networks grown by chemical vapour deposition, *Nat. Mater* 10 (2011) 424e428.
- [13] Z.J. Fan, Y. Liu, J. Yan, G.Q. Ning, Q. Wang, T. Wei, et al., Template-directed synthesis of pillared-porous carbon nanosheet architectures: high-performance electrode materials for supercapacitors, *Adv. Energy Mater* 2 (2012) 419e424.
- [14] C.J. Cui, W.Z. Qian, Y.T. Yu, C.Y. Kong, B. Yu, L. Xiang, et al., Highly electroconductive mesoporous graphene nanofibers and their capacitance

- performance at 4 V, *J. Am. Chem. Soc.* 136 (2014) 2256e2259.
- [15] D.F. Sun, J. Yang, X.B. Yan, Synthesis and electrochemical biosensing properties of hierarchically porous nitrogen-doped graphene microspheres, *Chem-ElectroChem* 2 (2015) 348e353.
- [16] Z.J. Fan, J. Yan, G.Q. Ning, T. Wei, L.J. Zhi, F. Wei, Porous graphene networks as high performance anode materials for lithium ion batteries, *Carbon* 60 (2013) 558e561.
- [17] J.L. Shi, C. Tang, H.J. Peng, L. Zhu, X.B. Cheng, J.Q. Huang, et al., 3D mesoporous graphene: CVD self-assembly on porous oxide templates and applications in high-stable Li/S batteries, *Small* 11 (2015) 5243e5252.
- [18] Z.Y. Lyu, D. Xu, L.J. Yang, R.C. Che, R. Feng, J. Zhao, et al., Hierarchical carbon nanocages confining high-loading sulfur for high-rate lithium-sulfur batteries, *Nano Energy* 12 (2015) 657e665.
- [19] M.-Q. Zhao, Q. Zhang, J.-Q. Huang, G.-L. Tian, J.-Q. Nie, H.-J. Peng, et al., Unstacked double-layer templated graphene for high-rate lithium-sulphur batteries, *Nat. Commun.* 5 (2014) 3410.
- [20] J.-L. Shi, G.-L. Tian, Q. Zhang, M.-Q. Zhao, F. Wei, Customized casting of unstacked graphene with high surface area ($>1300\text{ m}^2\text{ g}^{-1}$) and its application in oxygen reduction reaction, *Carbon* 93 (2015) 702e712.
- [21] G.L. Tian, Q. Zhang, M.Q. Zhao, H.F. Wang, C.M. Chen, F. Wei, Fluidized-bed cvd of unstacked double-layer templated graphene and its application in supercapacitors, *AIChE J.* 61 (2015) 747e755.
- [22] J.R. Dahn, A.K. Sleight, H. Shi, J.N. Reimers, Q. Zhong, B.M. Way, Dependence of the electrochemical intercalation of lithium in carbons on the crystal structure of the carbon, *Electrochim Acta* 38 (1993) 1179e1191.
- [23] J. Dahn, T. Zheng, Y. Liu, J. Xue, Mechanisms for lithium insertion in carbonaceous materials, *Science* 270 (1995) 590.
- [24] D.A. Stevens, J.R. Dahn, The mechanisms of lithium and sodium insertion in carbon materials, *J. Electrochem Soc.* 148 (2001) A803eA811.
- [25] Z. Chen, Q. Wang, K. Amine, Improving the performance of soft carbon for lithium-ion batteries, *Electrochim Acta* 51 (2006) 3890e3894.
- [26] Y.-N. Jo, M.-S. Park, E.-Y. Lee, J.-G. Kim, K.-J. Hong, S.-I. Lee, et al., Increasing reversible capacity of soft carbon anode by phosphoric acid treatment, *Electrochim Acta* 146 (2014) 630e637.
- [27] D.H. Everett, J.C. Powl, Adsorption in slit-like and cylindrical micropores in the Henry's law region. A model for the microporosity of carbons, *J. Chem. Soc. Faraday Trans.* 72 (1976) 619e636.
- [28] Z.Q. Li, C.J. Lu, Z.P. Xia, Y. Zhou, Z. Luo, X-ray diffraction patterns of graphite and turbostratic carbon, *Carbon* 45 (2007) 1686e1695.
- [29] L.M. Malard, M.A. Pimenta, G. Dresselhaus, M.S. Dresselhaus, Raman spectroscopy in graphene, *Phys. Rep.* 473 (2009) 51e87.
- [30] T.I.T. Okpalugo, P. Papakonstantinou, H. Murphy, J. McLaughlin, N.M.D. Brown, High resolution XPS characterization of chemical functionalised mwcnts and swcnts, *Carbon* 43 (2005) 153e161.
- [31] M. Thommes, J. Morell, K.A. Cychosz, M. Fr6ba, Combining nitrogen, argon, and water adsorption for advanced characterization of ordered mesoporous carbons (CMKS) and periodic mesoporous organosilicas (PMOS), *Langmuir* 29 (2013) 14893e14902.
- [32] Y. Jiao, Y. Zheng, M. Jaroniec, S.Z. Qiao, Design of electrocatalysts for oxygen- and hydrogen-involving energy conversion reactions, *Chem. Soc. Rev.* 44 (2015) 2060e2086.
- [33] D.S. Yu, L. Wei, W.C. Jiang, H. Wang, B. Sun, Q. Zhang, et al., Nitrogen doped holey graphene as an efficient metal-free multifunctional electrochemical catalyst for hydrazine oxidation and oxygen reduction, *Nanoscale* 5 (2013) 3457e3464.
- [34] S.Y. Wang, L.P. Zhang, Z.H. Xia, A. Roy, D.W. Chang, J.B. Baek, et al., Bcn graphene as efficient metal-free electrocatalyst for the oxygen reduction reaction, *Angew. Chem. Int. Ed.* 51 (2012) 4209e4212.
- [35] D.-W. Wang, D.S. Su, Heterogeneous nanocarbon materials for oxygen reduction reaction, *Energy Environ. Sci.* 7 (2014) 576e591.
- [36] L. Dai, Y. Xue, L. Qu, H.-J. Choi, J.-B. Baek, Metal-free catalysts for oxygen reduction reaction, *Chem. Rev.* 115 (2015) 4823e4892.
- [37] K.H. Wu, D.W. Wang, I.R. Gentle, Revisiting oxygen reduction reaction on oxidized and unzipped carbon nanotubes, *Carbon* 81 (2015) 295e304.
- [38] S.K. Bikkarolla, P. Cumpson, P. Joseph, P. Papakonstantinou, Oxygen reduction reaction by electrochemically reduced graphene oxide, *Faraday Discuss.* 173 (2014) 415e428.
- [39] W. Wei, Y. Tao, W. Lv, F.Y. Su, L. Ke, J. Li, et al., Unusual high oxygen reduction performance in all-carbon electrocatalysts, *Sci. Rep.* 4 (2014) 6289.
- [40] A. Shen, Y. Zou, Q. Wang, R.A.W. Dryfe, X. Huang, S. Dou, et al., Oxygen reduction reaction in a droplet on graphite: Direct evidence that the edge is more active than the basal plane, *Angew. Chem. Int. Ed.* 53 (2014) 10804e10808.